A MONTE CARLO MODEL OF STOCHASTIC ALPHA PARTICLE MICRODOSIMETRY IN 3D MULTICELLULAR AGGREGATES

A Dissertation
Presented to
The Academic Faculty

By

Tahir I. Yusufaly

In Partial Fulfillment
of the Requirements for the Degree
Master of Science in the
Department of Medical Physics

Georgia Institute of Technology

December 2021

A MONTE CARLO MODEL OF STOCHASTIC ALPHA PARTICLE MICRODOSIMETRY IN 3D MULTICELLULAR AGGREGATES

Approved by:

Dr. C-K Chris Wang, Advisor
Department of Medical Physics
Georgia Institute of Technology

Dr. Eric Elder
Department of Medical Physics
Georgia Institute of Technology

Dr. Tianye Niu
Department of Medical Physics
Georgia Institute of Technology

Dr. Steve Biegalski
Department of Medical Physics
Georgia Institute of Technology

Date Approved: May 17, 2021

For Anaan.

ACKNOWLEDGEMENTS

I would like to thank Dr. Chris Wang for his advice and mentorship in the preparation of this thesis. I would also like to thank Dr. Tianye Niu, Dr. Eric Elder and Dr. Steve Biegalski for agreeing to serve on my committee. Finally, I would like to thank my family, especially my wife Anaan, my daughter Azhari, my parents Dr. Imdad and Dr. Yasmin Yusufaly, and my sister Dr. Sara Yusufaly, for their unconditional love and support.

SUMMARY

Targeted alpha therapy (TAT) is an emerging new approach to radionuclide therapy, and promises to be especially valuable in the treatment of metastatic disease and radioresistant tumors. However, the dosimetry of TAT presents challenges not seen in photon therapy, due to uncertainties in the relative biological effectiveness (RBE) of alpha radiation.

One of the most dominant sources of this uncertainty is the stochasticity originating from the discrete nature of alpha particles, resulting in nonuniform cellular uptake patterns at low specific activities. Current approaches to alpha particle internal dosimetry, based on the MIRD formalism, typically assume that activity is uniformly distributed in subcellular compartments, with resulting absorbed dose distributions being unrealistically homogeneous and isotropic.

We develop a Monte Carlo generalization of the MIRD-based formalism that explicitly accounts for stochastic nonuniform localization of alpha emitters in a general 3D multicellular aggregate. In the limit of averaging over many replicates, our approach reduces to the MIRD-based one, which we verify by comparing our code's results with those of MIRDcell, a commonly used software for TAT dosimetry based on the MIRD formalism. At low specific activity, stochasticity manifests itself as an increase in cell survival beyond that expected from MIRD-based calculations, along with corresponding shifts in the generalized equivalent uniform dose. The magnitude of this effect strongly depends on the cellular localization of alpha emission, a parameter that can be experimentally controlled by altering the chemistry of the conjugate delivery vehicle of the radionuclide.

TABLE OF CONTENTS

LIST OF TABLES

LIST OF FIGURES

CHAPTER 1

INTRODUCTION

1.1 The Status Quo in Cancer Treatment

The standard-of-care in modern cancer treatment is built on the three pillars of surgery, radiotherapy and chemotherapy [1], as illustrated in Figure 1.1. Each modality has various strengths and weaknesses, and in practice, combination of multiple modalities is often necessary to optimize outcomes. Over the past century, advancements in this trifecta of modalities have resulted in dramatic improvements in both overall survival and quality of life in cancer patients.

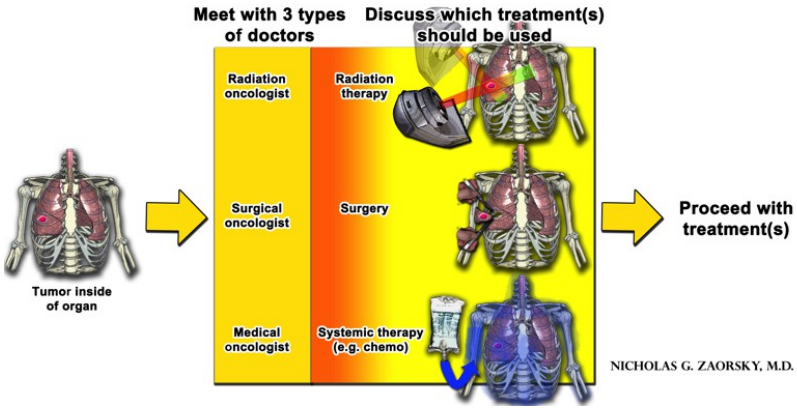

Figure 1.1: The standard of clinical cancer treatment today is built on the three pillars of radiation, surgery and chemotherapy. Courtesy of Nicholas G. Zaorsky [2].

However, despite this progress, cancer still remains a major global health burden, with a recent report [3] estimating 12.7 million new cases and 7.6 million new deaths in 2008. Prognosis is particularly poor for patients with metastatic disease [4], where the cancer has spread from the original primary site of induction to distal secondary sites throughout the body. In such cases, localized control at the primary site with surgery and radiotherapy is no longer sufficient to suppress the inherently systemic nature of the disease. Chemotherapy,

which circulates cytotoxic agents throughout the whole body, can slightly improve prognosis, but this efficacy is often limited because of the combination of normal tissue toxicity [5] and tumor chemoresistance due to cancer stem cells [6].

1.1.1 Emergence of Radiopharmaceutical Therapy (RPT)

Radiopharmaceutical therapy (RPT), which delivers radioactive atoms by conjugating them onto a pharmaceutical [7], has emerged as an alternative treatment modality. In contrast to more traditional radiotherapy, such as external beam, RPT is a systemic treatment that circulates throughout the body as in chemotherapy, as illustrated in Figure 1.2. This renders it particularly suitable for the treatment of metastatic disease. In addition, since RPT acts by emitting ionizing radiation that directly acts on the DNA target, its efficacy is far less sensitive to the specific details of biochemical pathways, enabling it to target tumors that are resistant to chemotherapy and similar 'biologic' treatments. This combination of features, among others, has resulted in RPT demonstrating favorable efficacy and low toxicity in clinical practice compared to other systemic treatments [8].

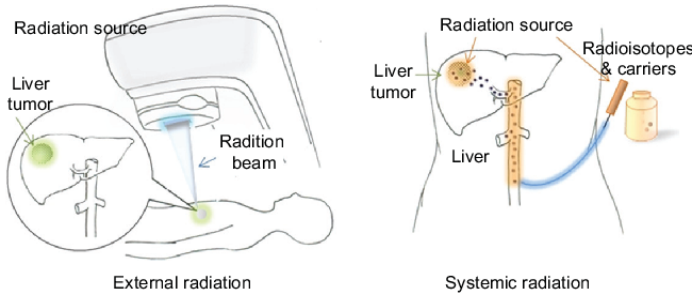

Figure 1.2: Compared to more traditional forms of radiotherapy, such as external beam, RPT results in a systemic whole-body distribution of radioactivity, rendering it potentially useful for the treatment of metastatic disease. Reprinted with Open Access permissions from Zhang, et al [9].

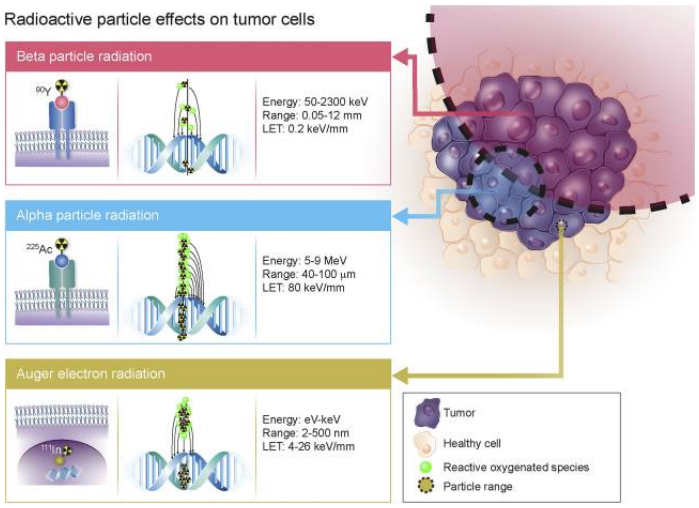

Figure 1.3: A comparison of therapeutic energy levels, linear energy transer (LET) and characteristic particle ranges for α, β and Auger electrons. Reprinted with permission from Poty, et al [10].

1.2 Targeted-α-Therapy (TAT): Opportunities and Challenges

1.2.1 Arguments for Using α-emitters in RPT

Within the space of RPT, the use of α-emitting radionuclides, known as targeted-α-therapy (TAT), has emerged as a particularly promising treatment subcategory. The reason for this can be illustrated by comparing the properties of α particle radiation to that of other commonly used radionuclide classes, such as β particles or Auger electrons, as shown in Figure 1.3.

Specifically, α particles at clinically relevant energies have an especialy high linear energy transfer (LET) compared to β particles, which renders them highly potent and effective at killing cells. This property is especially important when dealing with tumors that resist chemotherapy or other more traditional types of radiotherapy, since the high-LET potency effect is very robust to biological variability of the target cells.

In addition, clinically relevant α particles have a reasonable intermediate range in biological tissue on the order of 10-100 μm, in between that of the shorter-range Auger electrons and the longer-range β particles. This range is at the very useful 'sweet spot'

length scale of a few cell diameters. Thus, it is both short enough to enable sparing of organs at risk (OARs), but long enough to enable penetration of the tumor microenvironment.

1.2.2 The Relative Biological Effectiveness (RBE) Uncertainty Roadblock

However, despite this promise, roadblocks still remain in the clinical application of RPT in general, and TAT in particular. This is due in no small part to challenges associated with dosimetry and treatment planning compared to more traditional forms of radiotherapy. Specifically, while treatment planning for external beam and brachytherapy relies, for the most part, only on physical dosimetry metrics like the dose-volume histogram (DVH) or absorbed dose distribution, treatment planning for RPT places greater demands on radiobiological modeling in order to map physical dose to biological effects. The standard quantitative metric for such mapping is the relative biological effectiveness (RBE) [11, 12].

The RBE determined by measuring in vitro cell-survival curves at varying doses of that radiation, and comparing this cell survival curve to the corresponding one for X-rays. The RBE for a given radiation type is typically taken to be the ratio of the dose of that radiation required for a 0.1 cell survival fraction over the corresponding X-ray dose required for a 0.1 survival fraction. Typically this is done by fitting cell survival curves to a linear-quadratic formula [13]

$$\mathrm{SF} = e^{-\alpha D - \beta D^2} \tag{1.1}$$

where SF is the cell survival fraction, D is the dose, and α and β are radiobiological parameters.

For heavy particles, such as α emissions, however, a complication arises due to the large uncertainty, or variability, of RBE. An example of this is shown in Figure 1.4 for a squamous cell lung carcinoma cell line under both gamma and α radiation, for four different endpoints. We see that depending on the endpoint, the uncertainty of the RBE can be anywhere from 30 to 45 percent of the estimated value. This presents a problem for clinical use, since this high variability restricts the ability of physicians, dosimetrists and medical

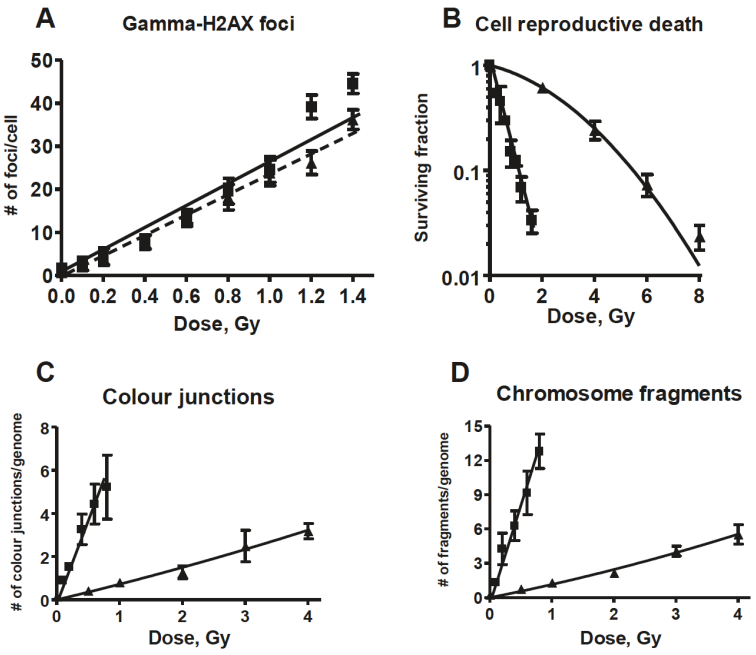

Figure 1.4: This figure, reprinted from [14], demonstrates the uncertainity of RBE from α particles (black squares) from an Am-241 source, relative to gamma rays (black triangles) from a Cs-137 source, for the SW-1573 sqaumous cell lung carcinoma cell line, and for four different biological endpoints.Calculated RBE values for DNA-DSBs, cell reproductive death, chromosome fragments and colour junctions are 1.0 ± 0.3, 14.7 ± 5.1, 15.3 ± 5.9 and 13.3 ± 6.0, respectively.

physicists to achieve the necessary consistency of high quality, accurate treatment planning required for safe and effective use.

1.2.3 Understanding RBE Uncertainty with Monte Carlo (MC) Calculations

The underlying reasons for the large RBE uncertainty of α particles are complex and multifaceted. Although a complete and rigorous mechanistic understanding is currently not possible, at a more general level the uncertainty of RBE can be understood as arising from the stochastic effects of how alpha particles deposit their energies at two different scale levels: (1) multicellular (i.e. the microdosimetry effect), and (2) subcellular (i.e. the nanodosimetry effect).

The microdosimetry effect, which is the focus of this thesis, arises from the stochastic and nonuniform uptake of -emitters at the cellular and sub-cellular levels. The nanodosimetry

effect, which is more complex and beyond the scope of this work, arises from the drastic change in LET of particles at the subcellular scale, results in variations in biological endpoints such as DNA double strand breaks (DSBs), chromosome aberrations, or cell survival.

Ultimately, whether due to microdosimetry or nanodosimetry effects, the uncertainty of RBE requires Monte Carlo (MC) calculations that explicitly incorporate randomness, whether in radiopharmaceutical uptake or in the track structure of α particles traversing the cell nucleus. Modeling the latter type of randomness requires very advanced MC algorithms and software, such as Geant4-DNA [15] and TOPAS-nBio [16], where the particle track structure calculations are fully carried and the subcellular structures (e.g. DNA, chromatin fibers, etc...) are modeled in great detail. The former type of randomness, however, is amenable to much simpler MC calculations that enable one to quantitatively analyze how the stochastic microdosimetry effect may affect the uncertainty of the RBE value for TAT.

1.3 Outline of this Thesis

With this in mind, the motivation behind this thesis is to develop, validate, and apply a MC model to characterize the effects of stochastic microdosimetry, due to nonuniform radionuclide uptake, on RBE. Chapter 2 starts by introducing the Medical Internal Radiation Dosimetry (MIRD) formalism, the currently accepted deterministic approach to internal dosimetry at the whole-organ level, as well as its limitations when dealing with microdosimetry. With this background, chapter 3 proceeds to develop a Monte Carlo generalization of the MIRD approach, validate it by comparing it with deterministic microdosimetry calculations and apply it to simulate stochastic microdosimetry in a multicellular aggregate. Chapter 4 reports the results of these simulations, including an analysis of the implications for various measures of biological effectiveness. Finally, chapter 5 concludes the thesis by summarizing the findings.

CHAPTER 2

FROM MIRD TO MONTE CARLO INTERNAL DOSIMETRY

2.1 The Medical Internal Radiation Dose (MIRD) Formalism

Internal dosimetry, the calculation of absorbed dose from internally deposited radionuclides, is a broad topic, a complete coverage of which is beyond the scope of this thesis. For a more thorough introduction, the reader is referred to the MIRD Primer [17]. Here, we only give a brief overview of the basics.

We take as our starting point for MIRD calculations, the cumulative time-integrated radionuclide activity

$$\tilde{A} = \int_{t=0}^{\infty} A(t) \tag{2.1}$$

, which can be calculated given the time-dependent activity $A(t)$ throughout the organs of the body, which in turn can be extracted via a combination of imaging and biokinetic physiological modeling.

Mathematically, if there are m separate *source* organs where radionuclide activity localized to, we may represent this as

$$\tilde{A}_s \ , \ s = 1, ..., m. \tag{2.2}$$

From each of these source organs emanates a certain amount of radioactivity. This radioactivity is then propagated throughout the body and deposited in various *target* organs as absorbed dose contributions. The total sum of all such contributions leads to a tabulation of absorbed doses $\bar{D}$. If there are n separate *target* organs, a corresponding mathematical representation of the target absorbed doses is

$$\bar{D}_t \ , \ t = 1, ..., n. \tag{2.3}$$

To estimate the target absorbed doses $\tilde{D}_t$ from the source cumulative activities $\tilde{A}_s$, we must determine, for each source-target pair, how the absorbed dose to a target from a given source varies with the cumulative activity in said source. In doing this, note that we must also consider 'self-doses', where the source organ and target organ are the same. A visual demonstration of this process is shown in Figure 2.1.

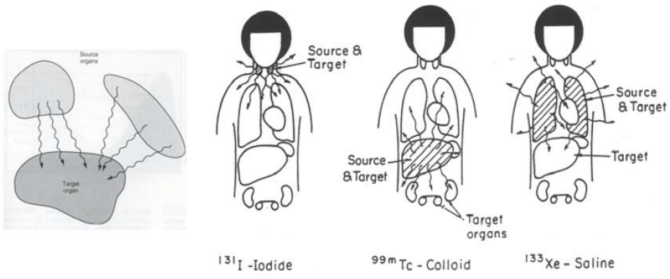

Figure 2.1: Diagrammatic illustration of the difference between 'source' and 'target' organs in the MIRD formalism. To the get the absorbed dose to a given target, we must calculate separately the total dose contributed from each source organ undergoing a given amount of cumulative activity. Reprinted from MIRD Primer [17].

To understand the mapping of cumulative activities to absorbed doses, let us without loss of generality consider a simplified example of two source organs, $s = 1, 2$, and one target organ, $t = 1$ that receives both 'self-dose' from its own radioactivity and 'cross-dose' from that of organ 2.

Over the time course of internal deposition, the total number of radioactive disintegration events that occur in organ 1 is equivalent to its cumulative time-integrated activity, $\tilde{A}_1$. Let there be p different types of disintegration events, and let each of them have a distinct average energy released per event, Δ_i, for $i = 1, ..., p$. Furthermore, let us assume that each separate disintegration product deposits a certain fraction $\phi_i(1 \leftarrow 1)$ of its total energy directly on organ 1, and that $\phi_1(1 \leftarrow 1)$ is independent of the total amount of activity. Then the average amount of energy deposited in organ 1 per disintegration event in organ 1, $\bar{E}(1 \leftarrow 1)/\tilde{A}_1$, is equal to the sum of the contributions of each of the separate

disintengration events,

$$\frac{\bar{E}(1 \leftarrow 1)}{\tilde{A}_1} = \sum_{i=1}^{p} \Delta_i \phi_i (1 \leftarrow 1). \tag{2.4}$$

If the mass of organ 1 is m_1, we can then use equation 2.4 to calculate the absorbed dose to organ 1 due to activity in organ 1, equals the average energy deposited divided by the mass

$$\bar{D}(1 \leftarrow 1) = \frac{\bar{E}(1 \leftarrow 1)}{m_1} = \tilde{A}_1 \frac{\sum_{i=1}^{p} \Delta_i \phi_i (1 \leftarrow 1)}{m_1}. \tag{2.5}$$

To determine how much absorbed dose organ 1 receives from organ 2, we proceed with a nearly identical argument. The only differences now are in: 1) the fractions $\phi_i(2 \leftarrow 1)$, which represent how much radioactivity from each disintegration type i 'leaks out' from organ 2 and ends up on organ, and 2) the value of the source activity, $\tilde{A}_2$. With those changes, we have

$$\bar{D}(1 \leftarrow 2) = \tilde{A}_2 \frac{\sum_{i=1}^{p} \Delta_i \phi_i (1 \leftarrow 2)}{m_1}. \tag{2.6}$$

Adding the contributions together, we see that the total dose to the target organ 1 is

$$\bar{D}_1 = \sum_{s=1}^{2} \bar{D}(1 \leftarrow s) = \sum_{s=1}^{2} \tilde{A}_s \frac{\sum_{i=1}^{p} \Delta_i \phi_i (1 \leftarrow s)}{m_1}. \tag{2.7}$$

Generalizing, for $s = 1, ..., m$ source organs, the absorbed dose to a target organ t is

$$\bar{D}_t = \sum_{s=1}^{m} \tilde{A}_s \left(\frac{\sum_{i=1}^{p} \Delta_i \phi_i (t \leftarrow s)}{m_t} \right). \tag{2.8}$$

The quantity in parentheses is so important that it is given a special name, the S-value,

$$S(t \leftarrow s) = \frac{\sum_{i=1}^{p} \Delta_i \phi_i (t \leftarrow s)}{m_t}. \tag{2.9}$$

S values are a compact quantitative representation of the absorbed dose to a given organ per unit cumulative activity in a given source organ, and are tabulated in the literature [18] for a variety of radiation types and organs.

Combining equations 2.3, 2.8 and 2.9, we end up with arguably the most important equation [11] in the Medical Internal Radiation Dose (MIRD) formalism,

$$D_t = \sum_{s=1}^{m} \tilde{A}_s S(t \leftarrow s) \ , \ t = 1, ..., n \tag{2.10}$$

This formalism makes many assumptions, one of the most glaring ones being the continuum approximation that the activities and absorbed doses in the source and target organs can be represented as uniform, homogeneous concentrations. A more realistic approach should take into account the microscale heterogeneity, due to the cellular microstructure of structures and organs, which in turn implies that the actual activity and absorbed dose will be correspondingly heterogeneous. Depending on the chemistry of the conjugate delivery vehicle, the radionuclide uptake may be preferentially localized, for example, at the cell membrane, at the cell cytoplasm, or at the nucleus. This heterogeneity effect is most pronounced for TAT due to the short ranges of alpha particles, and therefore needs to be investigated separately.

2.2 Towards Cellular Microdosimetry with MIRD-CELL and Monte Carlo

One of the simplest ways to account for this cellular microstructure is to treat each cell, with its corresponding nucleus, cytoplasm and membrane, as equivalent to a distinct microscale 'organ', as illustrated in Figure 2.2. Then, by determining the cellular and sub-cellular activity distributions, and given some distance-dependent S-values, we can extend the MIRD formalism of equation 2.10, by calculating the absorbed dose to individual 'target organ' cell nuclei, starting from a given cellular and sub-cellular distribution of time-integrated activities. This approach was worked out in detail in the 1990s [19, 20], and is currently the basis of state-of-the-art cellular microdosimetry calculations as implemented in the MIRD-CELL code [21].

While more precise than the initial MIRD formalism, the approach in MIRD-CELL still

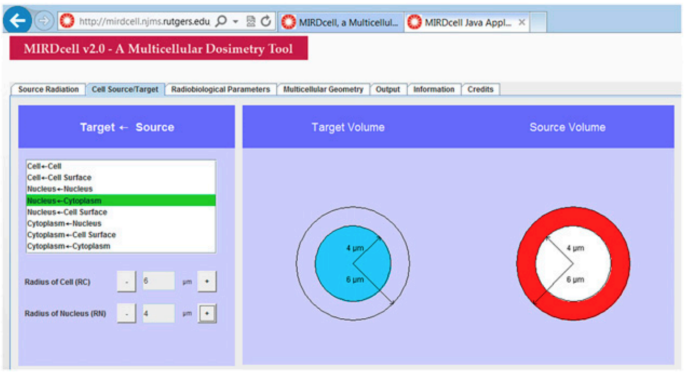

Figure 2.2: Diagrammatic illustration of the definition of cellular and subcellular 'organ' analogues in the MIRD-CELL formalism. Reprinted from MIRD Pamphlet 25 [21].

assumes that the activities and absorbed doses are large enough to be treated as a uniform continuum at the level of individual cells, membranes, or nuclei. For high specific activities, or large numbers of radionuclides per cell, this is not an unreasonable approximation. However, when the number of radionuclides per cell becomes sufficiently small, the continuum approximation can no longer be reasonably justified. A schematic illustration of this is shown in 2.3.

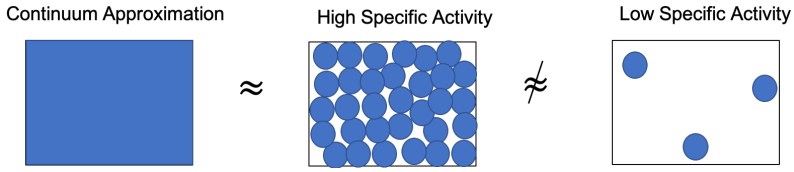

Figure 2.3: When discussing the concentration of discrete, finite-sized particles in a larger region, as is the case for, e.g., radionuclides in a subcelluar volume, distinctions must be made between the limits of high and low specific activities, or equivalently, concentration. At high specific activity, the concentration of radionuclides is enough that this density can be approximated as a uniform continuous field. However, at low specific activities, even though the likelihood of the particles being placed may be equal at all points in the volume, the low density invariably leads to a breakdown of the approximation of the homogeneity.

Accordingly, in order to properly account for this 'stochastic' effect arising from the discrete nature of the source carriers, a more rigorous Monte Carlo approach is needed.

CHAPTER 3

MONTE CARLO MODELING OF STOCHASTIC MICRODOSIMETRY

3.1 Building Blocks of the Monte Carlo Approach

To introduce the basics of the Monte Carlo approach to stochastic microdosimetry, let us start with a simple example of two cell nuclei, one a 'source' nucleus and the other a 'target' nucleus, as illustrated in Figure 3.1.

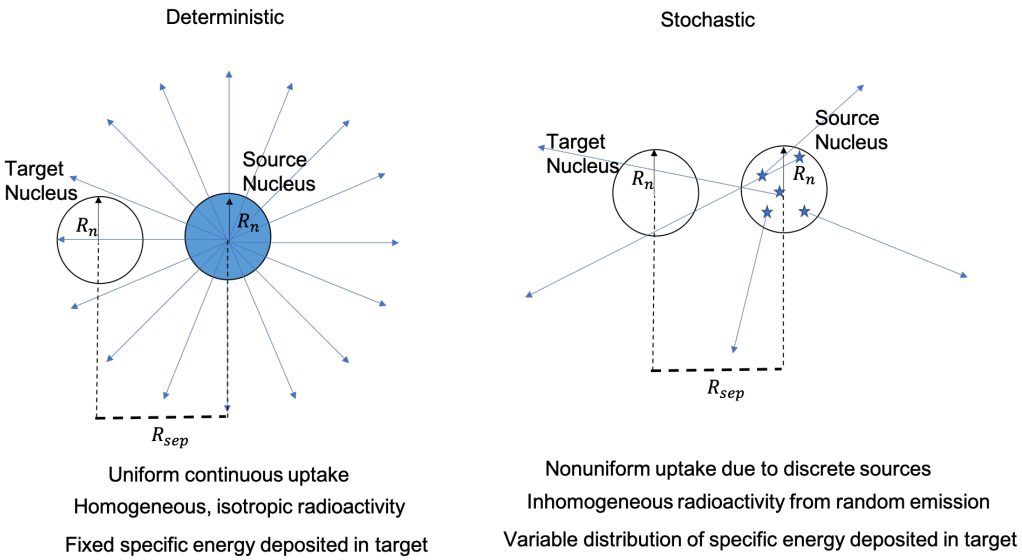

Figure 3.1: Converting a continuous activity to a discrete activity necessarily introduces random spatial inhomogeneity and anisotropic emission of radiation, due to quantization noise.

We see from Figure 3.1 that when we replace a uniform continuous activity concentration with a discrete distribution of sources, the finite size and number of the sources necessarily introduces some stochastic inhomogeneity in the subcellular activity distribution, as well as some corresponding stochastic anisotropy in the direction of radiation emission. These phenomena can be viewed as a specific example of the more general phenomenon known as 'quantization' noise [22].

For alpha particles, the cross dose due to straggling and secondary electron tracks is in general small enough to be negligible, such that we can reasonably assume the continuous slowing down approximation (CSDA) with no straggling [23]. As a consequence of this, emitted alpha radiation can be reasonably assumed to travel in a straight line, with a given range that increases with energy [24].

Thus, in order to quantify stochastic microdosimetry effects due to nonuniform distribution of discrete subcellular sources, we set up the Monte Carlo simulation so that, for a given spatial distribution of cells, the randomness is only in the positions of radionuclide activity and the direction of alpha particle emission. The remaining propagation of the alpha particles is assumed to be deterministic, enabling a direct integration of the energy deposited by the alpha particle in the parts of its track where it intersects with a cell nuclear target.

Explicitly, suppose we start with an initial estimate of a continuous uniform time-integrated activity in the source nucleus, $\tilde{A_N}$. If the rate constant for radioactive decay is λ, this corresponds to a total number of discrete disintegration 'source' radionuclides

$$N_{nuclide} = \tilde{A_N}/\lambda \, . \tag{3.1}$$

From our Monte Carlo simulation, we are looking to calculate the specific energy deposited in the target nucleus, z, due to all $N_{nuclide}$ of these sources. We start with setting $z = 0$, and initializing a counter variable i = 1. Then proceed as follows:

1. Randomly place a radionuclide, with a uniform probability distribution, at some point in the spherical source nucleus.

2. Assign a direction of emission for the alpha particle randomly, assuming an isotropic probability distribution for this direction.

3. Determine if the resulting 'straight-line' alpha particle track, as determined from step 2, intersects the central target nucleus. If it does, find r_{enter} and r_{exit}, the distances at

which the particle enters and exits the nucleus. If it does not, set the energy deposited in the target nucleus by this source to 0, $z_i = 0$, and skip to step 5.

4. Integrate the linear stopping power (using water-based values) from r_{enter} to r_{exit} to get the energy deposited in the target nucleus by this source, and divide it by the nuclear mass to get the specific energy z_i.

5. Add z_i to the total tally of specific energy, $z \to z + z_i$.

6. If $i = N_{nuclide}$, end calculation; otherwise, update $i \to i + 1$ and go back to step 1.

This simulation can then be repeated with the same nuclear geometry and parameters many times to generate a statistical distribution of specific energy (DSE) at the central target nucleus. Steps 5 and 6 of the above procedure are straightforward, but the first 4 steps merit more detailed explanation.

3.1.1 Random 3D Source Placement

Without loss of generality, and for the sake of simplicity, let us assume the source nucleus is centered on the origin. We reminder the reader of the definition of spherical polar coordinates in Figure 3.2. A point in space is defined by a distance from the origin r, a polar angle θ and an azimuthal angle ϕ.

In spherical polar coordinates, the volume of our nucleus is defined by the set of points

$$r \in [0, R_N] \tag{3.2}$$

$$\theta \in [0, \pi] \tag{3.3}$$

$$\phi \in [0, 2\pi]. \tag{3.4}$$

We need to sample a point randomly within this volume, in a way such that any point inside the nucleus is equally likely to be sampled. Naively, once might be tempted to just sample r, θ, ϕ uniformly from within their respective intervals. However, this is incorrect,

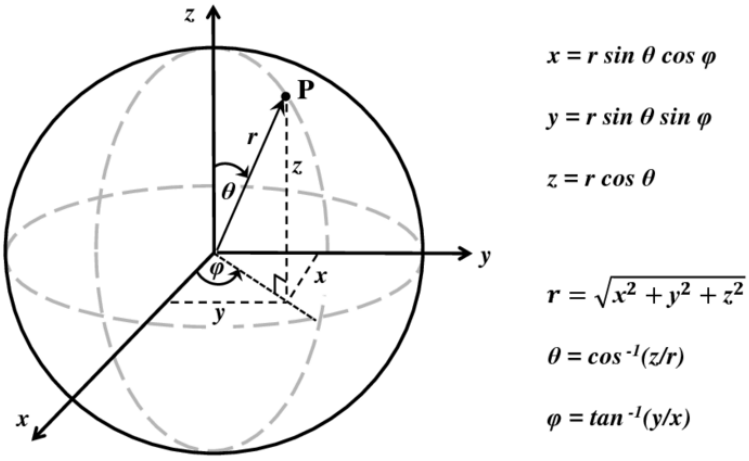

Figure 3.2: Recall the convention for spherical polar coordinates, including their relation to Cartesian coordinates.

as such an approach oversamples points both close to the origin and in the vicinity of the north and south poles. To understand how to do the sampling properly, it is instructive to inspect the volume integral for the nuclear sphere. Recall the definition of the differential volume element in spherical polar coordinates

$$dV = r^2 \sin(\theta) dr d\theta d\phi. \tag{3.5}$$

The volume of the nucleus, then, can be rewritten as

$$\begin{aligned} \int\int\int dV = \int_0^{R_N} r^2 dr \int_0^{\pi} \sin(\theta) d\theta \int_0^{2\pi} d\phi \\ = \int_0^{R_N^3/3} d(r^3/3) \int_{-1}^{1} d(\cos(\theta)) \int_0^{2\pi} d\phi. \end{aligned} \tag{3.6}$$

Thus, in order to obtain a true uniform sampling within the sphere, only ϕ can be simply set equal to a random number between 0 and 2π as we might have done naively. To sample r, we must set $r^3/3$ equal to a random number between 0 and $R_N^3/3$ and then solve for r. Similarly, to sample θ, we must set cos(θ) equal to a random number between -1 and 1 and solve for θ.

Note that this process is straightforwardly generalizable for arbitary non-spherical geometries. For example, if we want to constrain our radius to be between two values r_{min} and r_{max}, we would just sample a random number between $r_{min}^3/3$ and $r_{max}^3/3$ before solving for r. Such a situation would arise, for example, if we wanted to simulate scenarios where the radiopharmaceutical is not uniformly distributed throughout the entire cellular or nuclear volume, but is localized near the cell membrane surface.

3.1.2 Random Isotropic Emission

The determination of a random direction of emission, for the most part, follows almost directly from the logic used in the previous step. We seek to determine a random polar angle $\theta_{emission}$ and a random azimuthal angle $\phi_{emission}$ of emission. So again, we set cos($\theta_{emission}$) equal to a random number between -1 and 1 and solve for $\theta_{emission}$. $\phi_{emission}$ meanwhile is just set to a random number between 0 and 2π.

3.1.3 Calculating Intersection with the Target Nucleus

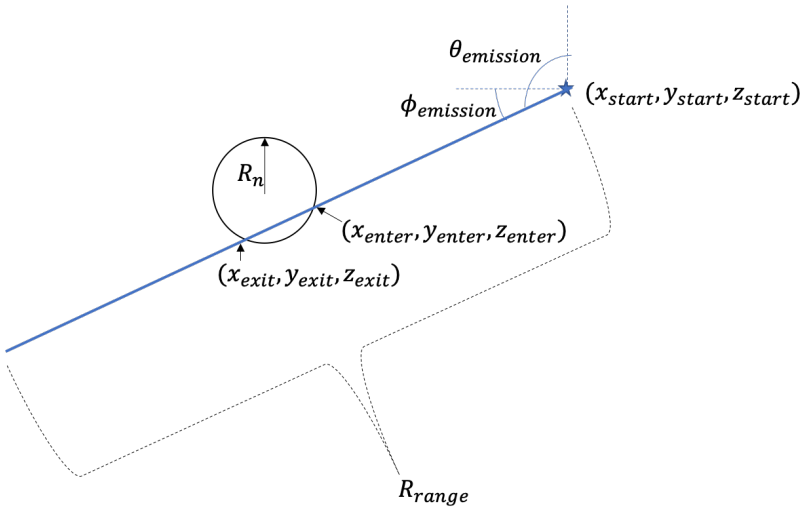

Figure 3.3: The schematic setup for calculating the intersection of an emitted alpha particle with the nuclear target.

Let us now revert back to our initial coordinate system setup, where the target nucleus is centered at the origin. Up to this point, we have established a way to determine the specific

location in space where the alpha emitter is emitted, let us call it the start point, with coordinates $\vec{r}_{start} = (x_{start}, y_{start}, z_{start})$. We also have a framework in place to determine a random direction of emission, as specified by the pair of angles $(\theta_{emission}, \phi_{emission})$. A visual illustration of this setup is shown in Figure 3.3.

We note from Figure 3.3 that, in addition to the variables already mentioned above, we also have an additional new variable, the range of the alpha particle R_{range}. To determine the value of R_{range}, we will need to know the energy of the emitted alpha particle. We can then find the corresponding range using a 'look-up' table of energy-range pairs extracted from the NIST database for CSDA ranges of alpha particles in liquid water [25]. A graph of this energy-range table is shown in Figure 3.4.

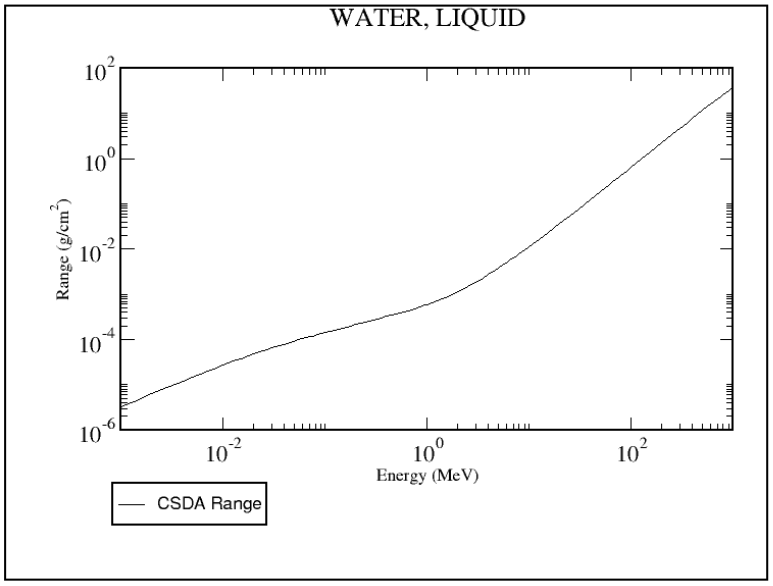

Figure 3.4: Energy-CSDA Range of alpha particles in liquid water, from NIST.

With this setup in place, let us proceed to briefly describe how to determine whether or not the alpha particle intersects with the target nucleus. We start by specifying a parametric formula for the alpha particle track

$$(x(r), y(r), z(r)) = (x_{start}, y_{start}, z_{start}) +$$
$$r(\sin(\theta_{emission})\cos(\phi_{emission}), \sin(\theta_{emission})\sin(\phi_{emission}), \cos(\theta_{emission}))\ ,$$
$$0 \leq r \leq R_{range}. \quad (3.7)$$

To determine if this line segment intersects the target, look to identify values of r for which the distance of $(x(r), y(r), z(r))$ from the origin equals the nuclear radius R_n,

$$R_n = \sqrt{x(r)^2 + y(r)^2 + z(r)}. \quad (3.8)$$

We will not go into the detailed algebra of how to solve this equation, but more information can be found in the code in the Appendix. For now, suffice it to say that we may check to see if there exist two real solutions to the equation $r_{enter} \leq r_{exit}$. If so, we can then check to see if $r_{exit} \leq R_{range}$, and if so, the alpha particle enters the target at r_{enter} and exits at r_{exit}. If $r_{enter} \leq R_{range} \leq r_{exit}$, then the alpha particle enters the nucleus, but dissipates away all its energy before exiting, so we then set $r_{exit} = R_{range}$. Finally, if $R_{range} < r_{enter}$, or if no real solutions exist, then the alpha particle track does not intersect the target, and the total specific energy deposited is 0.

3.1.4 Linear Stopping Power Integration

Finally, given the entry and exit distances, r_{enter} and r_{exit}, along with the initial alpha particle energy and range R_{range}, our remaining step is to integrate the stopping power to calculate how much energy is deposited in the target nucleus. Rather than do the integration directly, we will just use a clever conservation of energy argument. When the alpha particle enters the nucleus, its range at that point is just $R_{range} - r_{enter}$. Using the look-up table and plot in Figure 3.4, we can map any range R, via a one-to-one functional mapping $E(R)$, onto a corresponding energy E. Thus, the energy of the alpha particle as it enters is

$E_{enter} = E(R_{range} - r_{enter})$. Via an analogous argument, the energy of the alpha particle as it exits is $E_{exit} = E(R_{range} - r_{exit})$. Note that in the case where $R_{range} = r_{exit}$, meaning the alpha particle stops inside the target, $E_{exit} = E(0) = 0$.

By conservation of energy, then, the difference in energy between entry and exit equals the energy deposited in the target, $\Delta E = E_{enter} - E_{exit}$. To convert this to a specific energy, we just divide by the mass of the nucleus, m_N. If we take nucleus as having a uniform mass density ρ_N (often taken to be the value of water, 1 g/cm^3), then $m_N = \rho_N(4\pi r_N^3/3)$ and the specific energy deposited is $\Delta E/m_N$.

Once this is repeated for all the radionuclides, we then tally the specific energy deposited in the target nucleus. This simulation can then be repeated with the same initial geometry and parameters many times to generate a statistical distribution of specific energy (DSE) at the central target nucleus.

3.2 Single-Nucleus Calculation and Comparison with MIRD-CELL

In the limit of averaging over many replicates, the average specific energy should agree well with the predicted deterministic absorbed dose, as based on the MIRD-CELL formalism. To validate this, we run a simple test calculation simulating the alpha decay of an Ac-225 radiopharmaceutical, which emits an alpha particle with energy 5.93 MeV with a half life of 10 days, or equivalently a rate constant of 0.0693 days^{-1}. We assume localized uptake of the radiopharmaceutical with uniform probability to a single source nucleus with radius R_n= 5 microns. For simplicity, let us also assume that the source nucleus and target nucleus are identical - in other words, $R_{sep} = 0$. A concise table summarizing all these specific parameters is shown in 3.1.

We run calculations with total numbers of alpha decays (or transitions) ranging from 0 to 2000, in increments of 250. This corresponds to initial activities ranging from 0 to 1.6*10^{-3} Bq, in increments of 2*10^{-4} Bq. For each activity, we run 1000 simulation replicates to get the distribution of specific energy, from which we can extract the average

Table 3.1: Parameters for single nuclear source Monte Carlo simulation, assuming an Ac-225 alpha decay scheme.

Parameter	Value	Units
Alpha Energy	5.93	MeV
Rate Constant λ	0.0693	day^{-1}
Nuclear Radius R_n	5	Microns
Nuclear Mass Density ρ_n	1	g/cm^3
Source-Target Separation R_{sep}	0	Microns

specific energy $\langle z \rangle$ and corresponding standard error.

The results of this calculation are shown in Figure 3.5, where we also show the corresponding results calcuated using MIRD-CELL. MIRD-CELL, being a deterministic code, does not give a distribution of specific energy, but instead reports an absorbed dose per cellular nucleus, which is equivalent to the average specific energy in our Monte Carlo calculation.

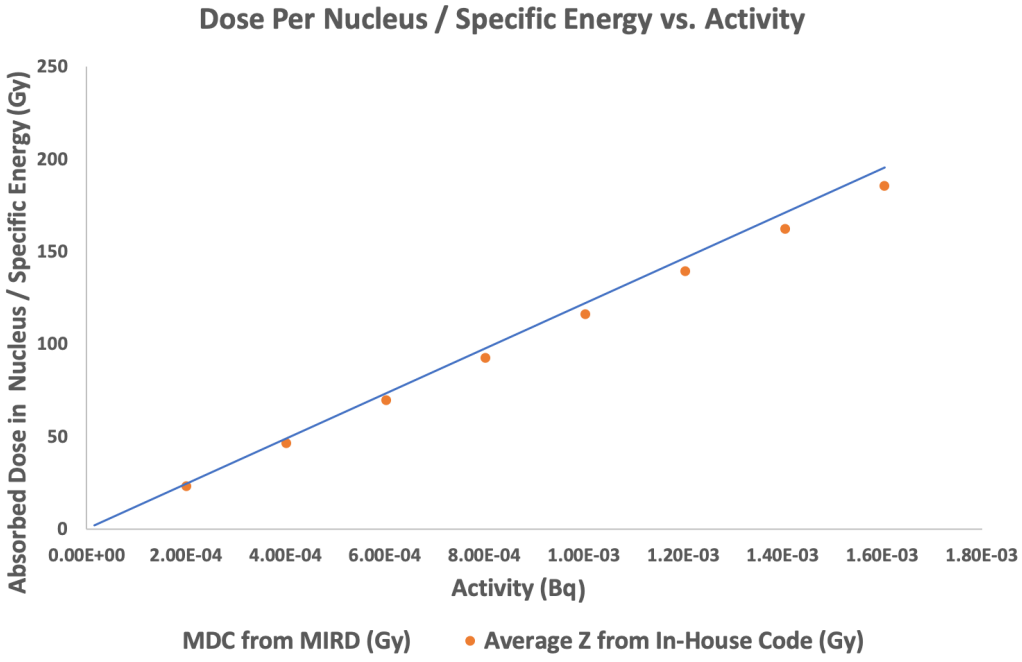

Figure 3.5: Scaling of the average specific energy, for Monte Carlo in-house calculations, with the total initial activity absorbed in the nucleus. For comparison we show the corresponding 'absorbed dose per nucleus' as extracted from MIRD-CELL. Note that standard error bars are present on the Monte Carlo data points, but are so small as to not be visible to the naked eye.

We see from this result that the Monte Carlo code agrees with the MIRD-CELL in that the average specific energy scales linearly with time-integrated activity. Furthermore, the magnitude of this slope is almost identical to the corresponding slope from MIRD-CELL. However, we do note that there is a slight difference. We suspect that this discrepancy might be due to the fact that we are using a different, more up-to-date set of energy-range data for the alpha particles, and that we are using a direct gridded interpolation fit of energy to range, while MIRD-CELL uses a parametric approximation to this fit. Nevertheless, the disagreement is small and inconsequential enough that we can safely conclude that the result serves as an initial validation of our method. With this in hand we can now proceed to analyze some more sophisticated scenarios with more complex multicellullar geometries.

3.3 Monte Carlo Simulation of a Multicellular Aggregate

Having established the working principles of our Monte Carlo calculation, we will now apply it to analyze the radiobiological effects of stochasticity, particularly at low specific activity.

We perform our calculations in the context of a 3D multicellular aggregate. Each cell in the aggregate consists of two concetric spheres, the inner spherical radius being that of the nucleus and the outer spherical radius being that of the entire cell. A multicellular aggregate is then represented as a random packing of non-overlapping spherical cells, placed inside a 3D cubic simulation volume. This is illustrated schematically via a 2D projection in Figure 3.6

The parameters for the multicellular aggregate Monte Carlo simuation are listed in Table 3.2, where just as before, we assume an Ac-225 type decay. We choose 100 cells in a (128 μm)^3 box in order for the cells to have a volumetric packing density of 0.2, with a box size sufficiently large relative to the range of the alpha particle so that the dose to the central target cell nucleus is an accurate representation of the 'bulk' dose, without being modified by finite-size artifacts. Note that, in addition to parameters describing

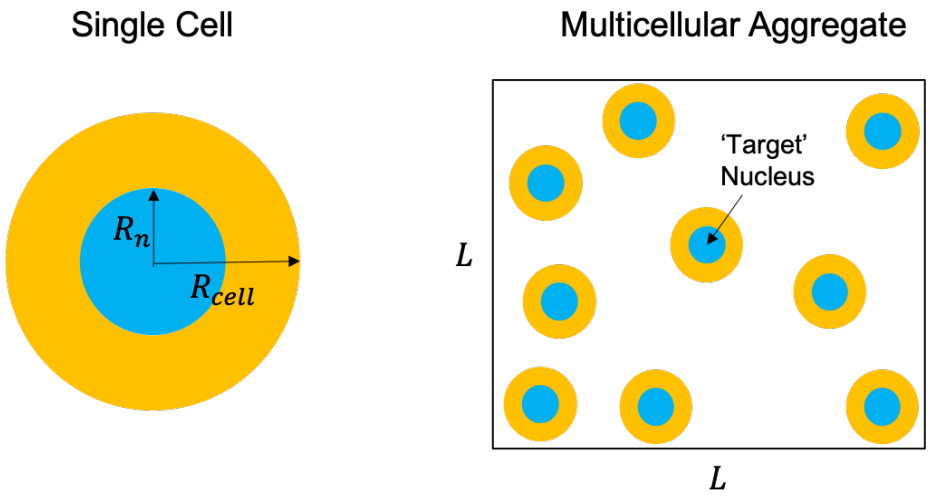

Figure 3.6: (Left) A single cell in the simulation is represented as a sphere (here just a circular cross sectin is shown) with a corresponding concentric inner sphere representing the nucleus. (Right) In a multicellular aggregate, a given number of cells are packed inside a cubic simulation volume (here just a square cross section is shown), and for the purposes of calcuating the distribution of specific energy and survival, we look at the energy deposited at a central 'target' nucleus at the center of the simulation box.

the radioactive decay and multicellular geometry, we also have two LQ radiobiological parameters α and β (which is typically safely assumed to be zero for alpha particles) describing how cell survival depends on the specific energy and specific energy squared, respectively. Quantitatively,

$$\text{SF} = e^{-\alpha * z - \beta * z^2} \tag{3.9}$$

where SF is the survival fraction and z is the specific energy. This exponential relationship will be important when analyzing the effects of stochasticity on the survival fraction distribution. Note that the above analysis assumes that only the direct damage to the cell nucleus causes cell death, neglecting various indirect DNA damage effects that may arise due to damage to non-cell nuclear targets, such as the mitochondria or cell surface.

We run three different simulations, representing distinct types of uptake scenarios, as illustrated schematically in Figure 3.7:

1. Uniform uptake within the nuclear volume.

Table 3.2: Parameters for multicellular Monte Carlo simulation, assuming an Ac-225 alpha decay.

Parameter	Value	Units
Energy	5.93	MeV
Rate Constant λ	0.0693	day^{-1}
Nuclear Radius R_n	5	Microns
Cell Radius R_{cell}	10	Microns
Number of Cells	100	N/A
Simulation Box Length	128	microns
Nuclear Mass Density ρ_n	1	g/cm^3
α	1.0	Gy^{-1}
β	0	Gy^{-2}

2. Uniform uptake within the entire cellular volume.

3. Uniform uptake on the cell membrane.

Figure 3.7: The three different patterns of radiopharmaceutical uptake considered.

These different scenarios can be viewed as approximately simulating the effects of altered chemistry of the delivery vehicle. Antibodies sometimes preferentially attach to the surface, for example, while nanoparticles sometimes localize directly to the nuclear target. For each different simulation scenario, we consider varying levels of time-integrated activity per cell. At each time-integrated activity, 1000 Monte Carlo replicates are performed in order to calculate a distribution of specific energies and survival fractions.

CHAPTER 4

RADIOBIOLOGICAL SIGNATURES OF STOCHASTICITY

4.1 Effects of Nonuniform Stochastic Uptake on Cell Survival

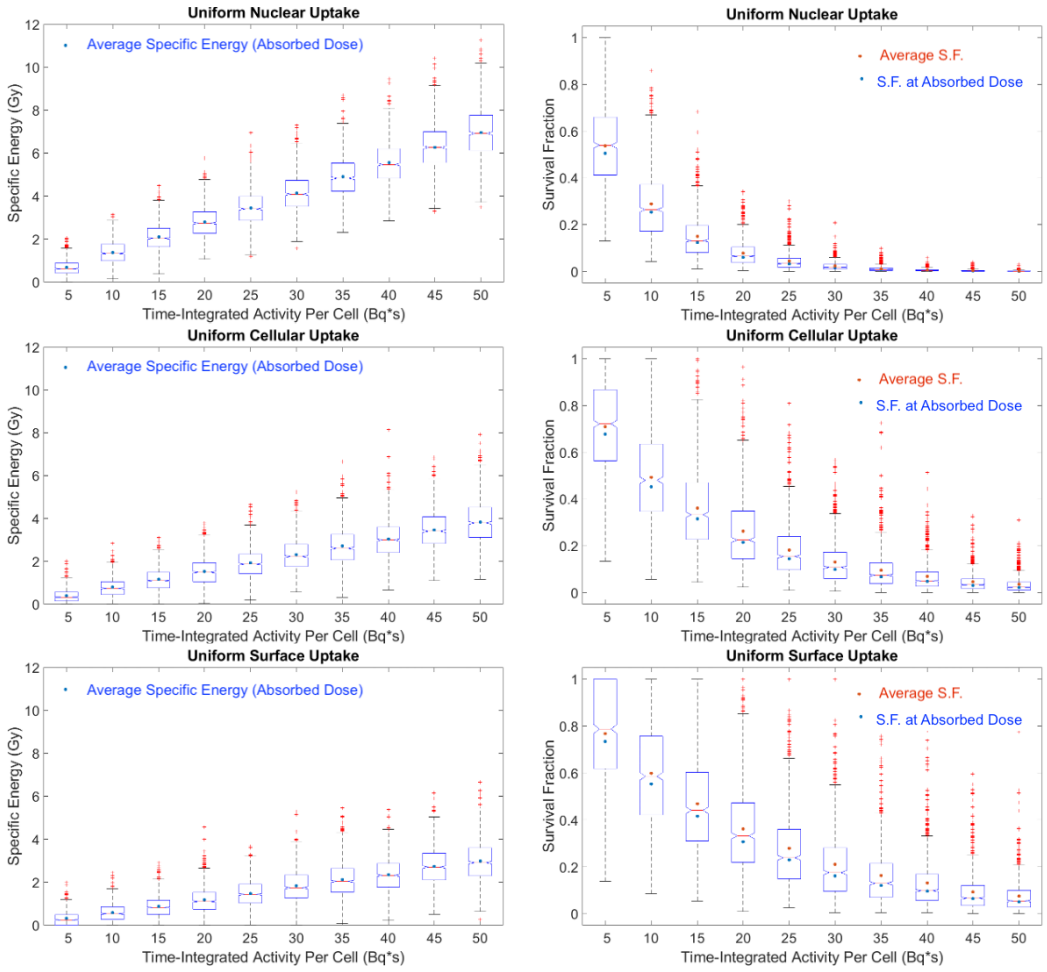

Figure 4.1: Histogram results showing the distribution of specific energy (DSE) and survival fraction (SF). For comparison, scatter point plots of the average DSE (i.e., the absorbed dose), the average SF and the SF evaluated at the absorbed dose are also displayed.

The primary results of the multicellular simulation are shown in Figure 4.1. This plot illustrates how the distribution of specific energy (DSE), and corresponding distribution of survival fraction (SF) based on the LQ model, change with the time-integrated activity.

Results are shown for each of the three uptake scenarios considered: uniform nuclear uptake, uniform cellular uptake and uniform surface uptake.

The results show that the DSE displays the same qualitative behavior that was observed for the single-nucleus simuation, with its average value scaling linearly with activity. The SF, meanwhile displays more complex nonlinear behavior. In part, this complex nonlinearity is due simply to the fact that LQ survival is an exponential function, so when the average specific energy, $\langle z \rangle$, if we relabel it the absorbed dose D, decreases, the LQ survival fraction at this average absorbed dose, $e^{-\alpha D}$, would naturally be expected to decrease exponentially.

However, a more careful analysis reveals that the average absorbed dose D is not the whole story. In particular, the stochastic fluctuations in the specific energy induce a nonzero overall shift in the average survival fraction. Mathematically,

$$\langle \text{SF} \rangle = \langle e^{-\alpha z} \rangle \neq e^{-\alpha \langle z \rangle} = e^{-\alpha D}, \tag{4.1}$$

and thus the magnitude of the stochastic shift can be quantified by defining the Jensen Gap [26], JG,

$$\text{JG} = \langle \text{SF} \rangle - e^{-\alpha D}. \tag{4.2}$$

And indeed, if we calculate $\langle \text{SF} \rangle$ and $e^{-\alpha D}$ from the MC data and plot them, as shown in Figure 4.1, we see a systematic nonzero shift.

4.1.1 Estimating the Jensen Gap Distribution with Boostrapping

While the results just described are a good qualitative first look at the effects of stochasticity, we would ultimately like to have a more rigorous quantification of the JG, including both its expected value and its uncertainty. In the language of statistics, we would like to estimate the sampling distribution of the JG.

A general way to do this is to use bootstrapping [27], as illustrated in Figure 4.2. Bootstrapping essentially works by taking a given sample of data, and resampling it with

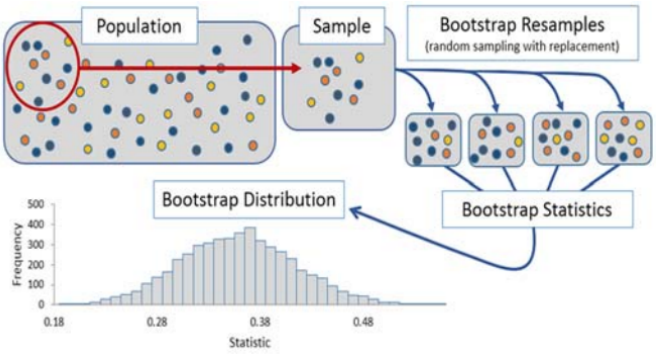

Figure 4.2: Visual explanation of bootstrapping to estimate the sampling distribution of a statistic. Reprinted with Open Access permissions from [27].

replacement over many replicates. At each replicate, a separate value of a desired sample statistic, whether it be mean, standard deviation, or in our case, the JG, is calculated. Repeating this over many replicates one may then estimate the sampling distribution.

We apply bootstrapping to our MC data for the multicellular simulation, doing 1000 bootstrap replicates, each with 1000 different resampled data points, and calculate the JG distribution accordingly. The corresponding bootstrap distribution of the JG is illustrated in Figure 4.3.

We see that the JG is always positive, meaning the average survival is always greater than the survival at the average dose. Mathematically, this is due to the convexity of the expoential function, and is entirely deducible as a consequence of a mathematical theorem known as Jensen's inequality [28]. Physically, it can be understood as arising from the fact that a nonuniform dose distribution results in some cells being overdosed, leading to an 'overkill' effect, while others are underdosed and correspondingly 'underkilled' [29], leading to a net overall increase in survival.

Analyzing the behavior of the JG, we see that its magnitude initially increases for very low activity, reaches a max, and then falls off. This is easy to understand by considering the extremes. At low activities, the SF is almost always 1, and thus stochasticity has trivially no effect, so the JG will be 0. At very high activity, the stochastic effects are also negligible, but this time because the deterministic approximation is increasingly exact in the limit of

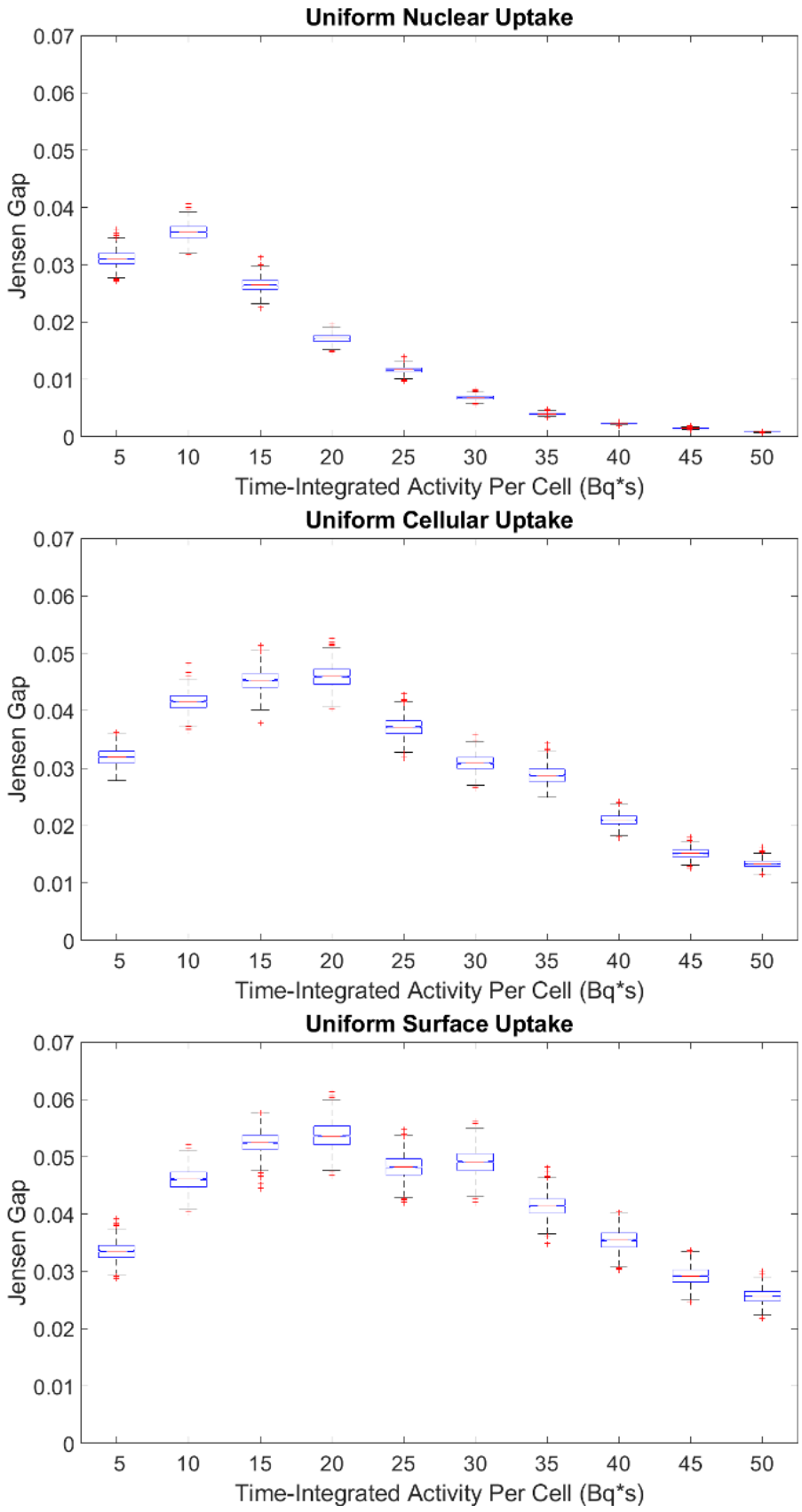

Figure 4.3: Bootstrap distributions of the Jensen Gap (JG) for varying activities and uptake patterns.

large numbers. Extrapolating between the two extremes we see that the gap must increase before it can decrease, so it is maximum at an intermediate level of activity.

We also see that uptake pattern has demonstrable consequences for differences in cell survival. Specfically, the more localized the uptake is towards the cell nucleus, the greater the effective cell kill per radionuclide decay. This can be understood as arising from the increased contribution of 'self-dose', which has a relatively high probability of cell kill, compared to 'cross-dose', which is more uncertain [30, 31, 32]. Thus, uptake by the cell nucleus is the most potent delivery, followed by whole cell uptake and finally surface uptake.

4.2 Effects on Generalized Equivalent Uniform Dose (gEUD)

The results for cell survival, while illuminating, ultimately must be related to therapeutic outcome, whether that be tumor control probability (TCP) or normal tissue complication probability (NTCP). At a fundamental, mechanistic level, understanding TCP and NTCP from the distribution of surviving cells is a question of understanding whether or not a certain critical fraction of the multicellular organ is destroyed. Such a de novo description is beyond the scope of this thesis. However, at a phenomenological level, we can gain some insight by analyzing the generalized equivalent uniform dose (gEUD), a commonly used empirical surrogate for TCP and/or NTCP [13]. gEUD is defined as

$$\text{gEUD} = (\sum_i v_i D_i^n)^{1/n} \tag{4.3}$$

where v_i is the fractional volume of an organ or tumor that receives dose D_i, and n is a structure-specific 'volume' parameter that measures how serial or parallel the structure is. If $n < 1$ the organ has a parallel architecture, meaning that the individual subvolumes are somewhat independent of each other. Thus, to disable the entire organ, it is sometimes necessary to disable all of its constitutent parts separately. A tumor is an extreme example

of a highly parallel 'organ' - disabling the tumor, or in other words controlling its spread, often requires killing each individual tumor cell separately. If $n > 1$, the organ instead has a serial architecture, and disabling one or a few substructures can be enough to disable the entire organ. A classic example of a serial organ is the spinal cord, where destroying any one 'link in the chain' can be enough to cause paralysis.

It is straightforward to apply the definition of gEUD to illustrate the stochastic microdosimetry effect. Here, we have a DSE, which can be viewed as a histogram of different specific energy levels z_i, each occuring with relative probability p_i. These can replace D_i and v_i, respectively, in Equation 4.3. Doing so, we see that

$$\text{gEUD} = (\sum_i p_i z_i^n)^{1/n} = \langle z^n \rangle^{1/n} \tag{4.4}$$

In other words, the gEUD is completely determined by the DSE, specifically by various moments of its distribution! And just as we used bootstrapping to quantify the sampling distribution of the JG statistic, so too can we use such an approach to estimate the sampling distribution of the gEUD. As in the case of JG, we run 1000 bootstraps with 1000 resamples per bootstrap. Results are shown in Figure 4.4, for a highly parallel case (n = -10), a reference 'mean dose' case (n = 1) and a highly serial case (n = 10).

4.2.1 Implications for Tumor Control and Normal Tissue Complication

It is informative to compare Figure 4.4 to the corresponding DSE plots shown in Figure 4.1. We see that for parallel (n = -10), mean-dose-weighted (n = 1) and serial (n = 10) architectures, the gEUD behaves, to a first approximation, like the minimum, mean and maximum values of the DSE, respectively. While the n = 1 case is somewhat generic, the other two merit some more commentary.

For a strongly parallel organ, such as a tumor, breakdown of the entire unit requires breakdown of every individual functional subunit. So, the probability of tumor control

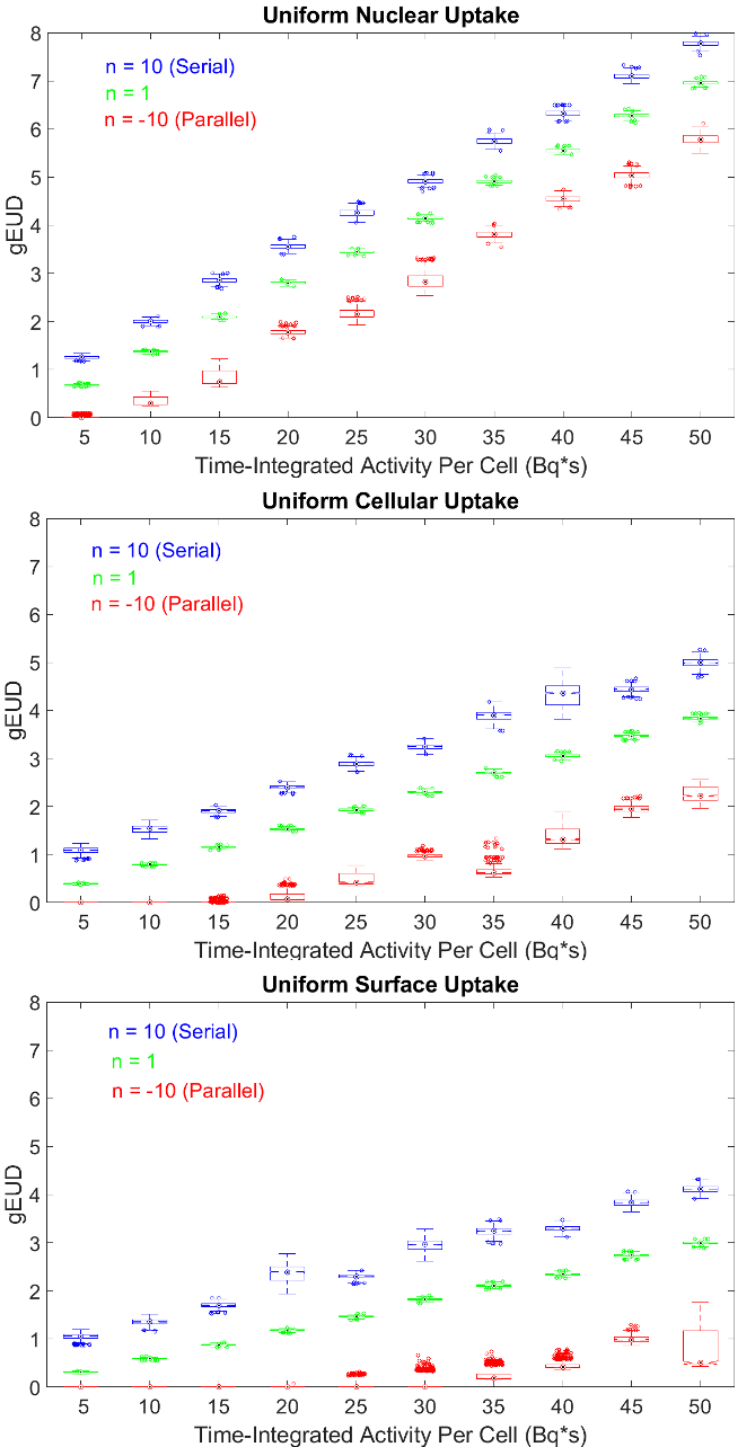

Figure 4.4: Bootstrap distributions of various gEUDs, as a function of specific activity and uptake pattern.

is only as good as the smallest probability of killing an individual cell. In other words, the efficacy is limited by the coldest spot in the dose distribution. For sufficiently large time-integrated activity, the concentration of radionuclides and resulting dose distribution is large and homogeneous enough to make this effect negligibly small. However, as the time-integrated activity decreases, the chances of at least one cell randomly getting zero specific energy increases, causing the gEUD to somewhat abruptly drop to near zero. Note that, just as we saw when analyzing the behavior of SF, the magnitude of this dip in gEUD is somewhat alleviated the more 'nuclear-localized' the radionuclide uptake pattern is.

For a strongly serial organ, on the other hand, the situation is reversed. Now, the toxicity of the treatment is determined by the maximum dose to an individual functional subunit, as it is the hot spots that determine the likelihood of any one link in the chain breaking down. Here, the effects of stochasticity manifest themselves as a slight increase in the gEUD at low specific activity. Indeed, as we see in Figure 4.4, a small nonzero activity leads to a disproportionately large increase in gEUD.

CHAPTER 5
CONCLUSIONS

In this thesis, we have developed and implemented a simple Monte Carlo model to investigate the effects of stochasticity in TAT dosimetry at the level of 3D multicellullar aggregates. We find that at low levels of time-integrated activity, the nonuniformity of the dose distribution leads to a Jensen Gap (JG), where the average survival fraction (SF) is greater than the expected SF at the average dose. Furthermore, when analyzing the generalized equivalent uniform dose (gEUD), we see that stochasticity manifests itself in an anomalously low gEUD for parallel organs and an anomalously high gEUD for serial organs.

We also found in simuations that the magnitude of this effect is strongly dependent on the localization and uptake pattern of the radionuclide. Uptake of radionuclides by the cell nucleus displays the least sensitivity to this stochasticity, since the 'self-dose' to the DNA target from the short-range alpha particles is the dominant variable responsible for cell death. For whole-cell uptake, the survival probability depends more on 'cross-dose' from adjacent cells, where the short range of the alpha particles and the discreteness of the multicellular geometry increase the importance of dose inhomogeneity. Finally, cell-surface uptake, which has the smallest contribution from 'self-dose' and the largest contribution from 'cross-dose', has the greatest sensitivity to stochastic effects.

These results indicate that uptake pattern significantly influences cell death and RBE. We can understand this pattern to be modulated by the chemical makeup of the radionuclide delivery vehicle. To a first approximation, if we consider two different types of drug carriers, antibodies and nanoparticles, antibodies can be viewed as preferentially localization at the cell surface, and nanoparticles can be viewed as preferentially localizing throughout the entire cellullar cytoplasm. However, in general, each new delivery vehicle needs to be separately characterized to more precisely define the pattern of subcellular localization.

Appendices

```
function DSE = totalTally(nReplicates,nCells, Width, CellRadius, nSources,
rMin,rMax, nuclearRadius, energy)
% INPUT:
%   nReplicates: number of monte carlo replicates
%   nCells:  Number of cells
%   Width:  Dimension of 3d box as [1 x 3] double vector in microns
%   CellRadius: Cell radii microns
%   nSources:  Number of radionuclide sources
%   rMin, rMax: range within cell where source could be (e.g., 0 to r_N is
%   nuclear localizatin, 0 to r_cell is whole cell localization, r_cell
%   wall to r_cellsurface is say cell surface localization)
%   nuclearRadius: Radius of spherical nucleus at the center (in microns)
%   energy: energy in MeV which can be used to estimate CSDA range of alpha
emissions
% OUTPUT:
%   DSE:      distributon of specific energy, in gray
DSE = [];

[~,~,energyRangeData] = xlsread('AlphaInWaterCSDARange.xlsx');

sampleEnergiesMeV = cell2mat(energyRangeData(2:end,1));
sampleRangesMicrons = cell2mat(energyRangeData(2:end,3));

energyToRangeInterpolant = griddedInterpolant(sampleEnergiesMeV,
sampleRangesMicrons);
rangeToEnergyInterpolant = griddedInterpolant(sampleRangesMicrons,
sampleEnergiesMeV);

for i = 1:nReplicates
    sourceCoordinates =
RandomSourcePositioning(nCells,Width,CellRadius,nSources,rMin,rMax);
    P = 0;
    for i = 1:nSources
        P = P +
Tally(sourceCoordinates(i,:),nuclearRadius,energy,energyToRangeInterpolant,ra
ngeToEnergyInterpolant);
    end

    % to convert to specific energy in gray:
    % assume mass density 1 g/cm^3 = 1E-15 kg/micron^3
    % and 1 MeV = 1.60281E-13 J

    DSE = horzcat(DSE,(P/((4*pi/3)*(nuclearRadius^3)))*(160.281));
end

end


function P = Tally(sourceCoord, nuclearRadius,
energy,energyToRangeInterpolant,rangeToEnergyInterpolant)
% INPUT:
%   sourceCoord:  The position of the alpha emitter, in Cartesian coordinates
(micrometer units) such
%   that the tally nucleus is at the center/origin.
%   nuclearRadius: Radius of spherical nucleus at the center (in microns)
```

```
%   energy: energy in MeV which can be used to estimate CSDA range of alpha
emissions
% OUTPUT:
%   P:      energy deposited in nucleus

% extract initial x,y,z coords of the source
xStart = sourceCoord(1);
yStart = sourceCoord(2);
zStart = sourceCoord(3);

range = energyToRangeInterpolant(energy); %get range
thetaRand = acos(2*rand - 1); %random polar angle, from 0 to pi radians;
phiRand = 2*pi*rand; %random azimuthal angle, from 0 to 2pi radians;

startingDistanceFromCenter = sqrt(xStart^2 + yStart^2 + zStart^2);

% now need to solve for entry radius rEnter and exit radius rExit
% (xStart + r*sin(thetaRand)*cos(phiRand))^2 +  (yStart +
% r*sin(thetaRand)*sin(phiRand))^2 + (zStart
% +r*cos(thetaRand))^2 = nuclearRadius^2

% r^2 + 2*(xStart*sin(thetaRand)*cos(phiRand) +
% yStart*sin(thetaRand)*sin(phiRand) + zStart*cos(thetaRand))*r +
% (xStart^2 + yStart^2 + zStart^2 - nuclearRadius^2) = 0

% r^2 + B*r + C = 0, C < 0
% B = 2*(xStart*sin(thetaRand)*cos(phiRand) +
yStart*sin(thetaRand)*sin(phiRand) + zStart*cos(thetaRand))
% C = startingDistanceFromCenter^2 - nuclearRadius^2

B = 2*(xStart*sin(thetaRand)*cos(phiRand) +
yStart*sin(thetaRand)*sin(phiRand) + zStart*cos(thetaRand));
C = startingDistanceFromCenter^2 - nuclearRadius^2;

rplus = (-B + sqrt(B^2 - 4*C))/2;
rminus = (-B - sqrt(B^2 - 4*C))/2;

if(imag(rplus) ~= 0) % complex r+/r- means it doesnt intersect sphere
    P = 0;
elseif(rplus < 0) % if r+ < 0 then it does not intersect in the direction of
emission
    P = 0;
elseif (rminus > range) % if r- > range, then it dissipates away before
entering nucleus
    P = 0;
elseif(rminus < 0) % if r- < 0 when r+ > 0, it means that the source emits
from within the target
    P = energy - rangeToEnergyInterpolant(range - rplus); % if by chance
range > r+, this will equal energy automatically
else % now only possibility is that it starts outside the nucleus but enters
it before dissipating away
    P = rangeToEnergyInterpolant(range - rminus) -
rangeToEnergyInterpolant(range - rplus);

End
```

```
function P = RandomSoucePositioning(nCells, Width, CellRadius, nSources,
rMin,rMax)
% INPUT:
%   nCells:  Number of cells
%   Width:  Dimension of 3d box as [1 x 3] double vector
%   CellRadius: Cell radii
%   nSources:  Number of radionuclide sources
%   rMin, rMax: range within cell where source could be (e.g., 0 to r_N is
%   nuclear localizatin, 0 to r_cell is whole cell localization, r_cell
%   wall to r_cellsurface is say cell surface localization)

% OUTPUT:
%   P:      [nSource x 3] matrix, source coordinates

cellCoordinates = GetRandomSpheres(nCells, Width, CellRadius);
P = [];

for i = 1:nSources

    randomCellCenter = cellCoordinates(randi(nCells),:); % random cell that
this source goes in
    randomDistance = rMin + (rMax-rMin)*(rand)^(1/3); % random distance of
source from cell center
    thetaRand = acos(2*rand-1); %random polar angle, from 0 to pi radians;
    phiRand = 2*pi*rand; %random azimuthal angle, from 0 to 2pi radians;

    % extract central x,y,z coords of the cell
    xStart = randomCellCenter(1);
    yStart = randomCellCenter(2);
    zStart = randomCellCenter(3);

    % use the random theta and phi, along with random distance to specify
    % source coordinates , converting spherical to Cartesian
    x = xStart + randomDistance*sin(thetaRand)*cos(phiRand);
    y = yStart + randomDistance*sin(thetaRand)*sin(phiRand);
    z = zStart + randomDistance*cos(thetaRand);

    P = vertcat(P,[x-Width/2,y-Width/2,z-Width/2]); %note, shifting it all so
that the center of the box is at the origin

end


function P = GetRandomSpheres(nWant, Width, Radius)
% INPUT:
%   nWant:  Number of spheres
%   Width:  Dimension of 3d box as [1 x 3] double vector
%   Radius: Radius of spheres
% OUTPUT:
%   P:      [nWant x 3] matrix, centers
P = zeros(nWant, 3);
P(1,:) = [Width/2,Width/2,Width/2];            % start with one sphere/cell
at the center
R2     = (2 * Radius) ^ 2;   % Squared once instead of SQRT each time
W      = Width - 2 * Radius; % Avoid interesction with borders
```

```
iLoop  = 1;                  % Security break to avoid infinite loop
nValid = 1;
while nValid < nWant && iLoop < 1e6
  newP = rand(1, 3) .* W + Radius;
  % Auto-expanding, need Matlab >= R2016b. For earlier versions:
  % Dist2 = sum(bsxfun(@minus, P(1:nValid, :), newP) .^ 2, 2);
  Dist2 = sum((P(1:nValid, :) - newP) .^ 2, 2);
  if all(Dist2 > R2)
    % Success: The new point does not touch existing sheres:
    nValid       = nValid + 1;  % Append this point
    P(nValid, :) = newP;
  end
  iLoop = iLoop + 1;
end
% Stop if too few values have been found:
if nValid < nWant
  error('Cannot find wanted number of points in %d iterations.', iLoop)
end
end
```

REFERENCES

[1] Z. Abbas and S. Rehman, "An overview of cancer treatment modalities," *Neoplasm*, vol. 1, pp. 139–157, 2008.

[2] *Cancer Treatments*, `https://www.cancerquest.org/sites/default/files/assets/image/tumor-treatment-options-zaorsky.jpg`, Accessed: 2021-03-29.

[3] J. Ferlay, H.-R. Shin, F. Bray, D. Forman, C. Mathers, and D. Maxwell Parkin, "Estimates of worldwide burden of cancer in 2008," *International Journal of Cancer*, vol. 127, no. 12, pp. 2893–2917, 2010.

[4] P. S. Steeg, "Tumor metastasis: Mechanistic insights and clinical challenges," *Nature Medicine*, vol. 12, pp. 895–904, 2006.

[5] R. M. Lowenthal and K. Eaton, "Toxicity of chemotherapy," *Hematology/Oncology Clinics*, vol. 10, no. 4, pp. 967–990, 1996.

[6] L. N. Abdullah and E. K.-H. Chow, "Mechanisms of chemoresistance in cancer stem cells," *Clinical and Translational Medicine*, vol. 2, no. 3, pp. 1–9, 2013.

[7] G. Sgouros, L. Bodel, M. R. McDevitt, and J. R. Nedrow, "Radiopharmaceutical therapy in cancer: Clinical advances and challenges," *Nature Reviews Drug Discovery*, vol. 19, pp. 589–608, 2020.

[8] M. R. Gill, N. Falzone, Y. Du, and K. A. Vallis, "Targeted radionuclide therapy in combined-modality regimens," *Lancet Oncology*, vol. 18, no. 7, e414–e423, 2017.

[9] L. Zhang *et al.*, "Delivery of therapeutic radioisotopes using nanoparticle platforms: Potential benefits in systemic radiation therapy," *Nanotechnology, Science and Applications*, vol. 3, pp. 159–170, 2010.

[10] S. Poty, L. C. Francesconi, M. R. McDevitt, M. J. Morris, and J. S. Lewis, "Alpha-Emitters for Radiotherapy: From Basic Radiochemistry to Clinical Studies - Part 1," *Journal of Nuclear Medicine*, vol. 59, no. 6, pp. 878–884, 2018.

[11] W. E. Bolch, K. F. Eckerman, G. Sgorous, and S. R. Thomas, "MIRD Pamphlet 21: A Generalized Schema for Radiopharmaceutical Dosimetry - Standardization of Nomenclature," *Journal of Nuclear Medicine*, vol. 50, no. 3, pp. 477–484, 2009.

[12] G. Sgouros *et al.*, "MIRD Pamphlet 22: Radiobiology and dosimetry of Alpha-Particle Emitters for Targeted Radionuclide Therapy," *Journal of Nuclear Medicine*, vol. 51, no. 2, pp. 311–328, 2010.

[13] X. A. Li *et al.*, "The Use and QA of Biologically Related Models for Treatment Planning," *Medical Physics*, vol. 39, no. 3, pp. 1386–1409, 2012.

[14] N. A. Franken *et al.*, "Comparison of RBE values of high-LET alpha-particles for the induction of DNA-DSBs, chromosome aberrations and cell reproductive death," *Journal of Nuclear Medicine*, vol. 51, no. 2, pp. 311–328, 2010.

[15] S. Incerti *et al.*, "The GEANT4-DNA Project," *International Journal of Modeling, Simulation and Scientific Computing*, vol. 1, no. 2, pp. 157–178, 2010.

[16] J. Schuemann *et al.*, "TOPAS-nBio: An Extension to the TOPAS Simulation Toolkit for Cellular and Sub-cellular Radiobiology," *Radiation Research*, vol. 191, no. 2, pp. 125–138, 2019.

[17] R. Loevinger, T. Budinger, and E. Watson, *MIRD Primer for Absorbed Dose Calculations*. New York, NY: The Society of Nuclear Medicine, 1991.

[18] L. Bouchet *et al.*, "MIRD pamphlet no. 15: Radionuclide s values in a revised dosimetrie model of the adult head and brain," *Journal of Nuclear Medicine*, vol. 40, no. 3, 62S–101S, 1999.

[19] S. Goddu, R. Howell, L. Bouchet, W. Bolch, and D. Rao, *Self Absorbed Dose per Unit Cumulated Activity for Selected Radionuclides and Monoergenetic Electron and Alpha Particle Emitters Incorporated into Different Cell Compartments*. Reston, VA: Society of Nuclear Medicine and Molecular Imaging, 1997.

[20] S. M. Goddu, R. W. Howell, and D. V. Rao, "Cellular Dosimetry: Absorbed Fractions for Monoenergetic Electron and Alpha Particle Sources and S-Values for Radionuclides Uniformly Distributed in Different Cell Compartments," *Journal of Nuclear Medicine*, vol. 35, no. 2, pp. 303–316, 1994.

[21] B. Vaziri, H. Wu, A. P. Dhawan, P. Du, and R. W. Howell, "MIRD Pamphlet 25: MIRDcell v2.0 Software Tool for Dosimetric Analysis of Biologic Response of Multicellular Populations," *Journal of Nuclear Medicine*, vol. 55, no. 9, pp. 1557–1564, 2014.

[22] R. M. Gray, "Quantization noise spectra," *IEEE Transactions on Information Theory*, vol. 36, no. 6, pp. 1220–1244, 1990.

[23] J. Poston, "Dosimetry," in *Encyclopedia of Physical Science and Technology (Third Edition)*, R. A. Meyers, Ed., Third Edition, New York: Academic Press, 2003, pp. 603–650, ISBN: 978-0-12-227410-7.

[24] J. C. Roeske and M. Hoggarth, "Alpha-particle monte carlo simulation for microdosimetric calculations using a commercial spreadsheet," *Physics in Medicine and Biology*, vol. 52, no. 7, pp. 1909–1922, 2007.

[25] *NIST ASTAR Database*, `https://physics.nist.gov/PhysRefData/Star/Text/ASTAR.html`, Accessed: 2020-09-03.

[26] S. Abramovich and L.-E. Persson, "Some new estimates of the 'Jensen gap'," *Journal of Inequalities and Applications*, vol. 39, pp. 1–9, 2016.

[27] E. Banjanovic and J. Osborne, "Confidence Intervals for Effect Sizes: Applying Bootstrap Resampling," *Practical Assessment, Research and Evaluation*, vol. 21, no. 5, pp. 1–20, 2016.

[28] D. Chandler, *Introduction to Modern Statistical Mechanics*. New York, NY: Oxford University Press, 1987.

[29] J. A. O'Donoghue, "Implications of Nonuniform Tumor Doses for Radioimmunotherapy," *Journal of Nuclear Medicine*, vol. 40, no. 8, pp. 1337–1341, 1999.

[30] S. M. Goddu, D. V. Rao, and R. W. Howell, "Multicellular Dosimetry for Micrometastases: Dependence of Self-Dose Versus Cross-Dose to Cell Nuclei on Type and Energy of Radiation and Subcellular Distribution of Radionuclides," *Journal of Nuclear Medicine*, vol. 35, no. 3, pp. 521–530, 1994.

[31] M. Eiblmaier, R. Andrews, R. Laforest, B. E. Rogers, and C. J. Anderson, "Nuclear Uptake and Dosimetry of 64-Cu-Labeled Chelator-Somatostatin Conjugates in an SSTr2-Transfected Human Tumor Cell Line," *Journal of Nuclear Medicine*, vol. 48, no. 8, pp. 1390–1396, 2007.

[32] R. W. Howell and P. V. Neti, "Modeling Multicellular Response to Nonuniform Distributions of Radioactivity: Differences in Cellular Response to Self-Dose and Cross-Dose," *Radiation Research*, vol. 163, no. 2, pp. 216–221, 2005.